Article

Partial Oxidation Synthesis of Prussian Blue Analogues for Thermo-Rechargeable Battery

Yutaka Moritomo [1,2,3,*] **, Masato Sarukura** [1] **, Hiroki Iwaizumi** [1,†] **and Ichiro Nagai** [2,‡]

1 Graduate School of Pure & Applied Science, University of Tsukuba, Tennodai 1-1-1, Tsukuba 305-8571, Ibaraki, Japan

2 Faculty of Pure & Applied Science, University of Tsukuba, Tennodai 1-1-1, Tsukuba 305-8571, Ibaraki, Japan

3 Research Center for Energy Materials Science (TREMS), University of Tsukuba, Tennodai 1-1-1, Tsukuba 305-8571, Ibaraki, Japan

* Correspondence: moritomo.yutaka.gf@u.tsukuba.ac.jp

† Current address: Research Institute of Material and Chemical Measurement, AIST, Umezono 1-1-1, Tsukuba 305-8569, Ibaraki, Japan.

‡ Current address: Faculty of Marine Technology, Tokyo University of Marine Science and Technology, Etchujima 2-1-6, Koto-ku, Tokyo 135-8533, Japan.

Abstract: A thermo-rechargeable battery or tertiary battery converts thermal energy into electric energy via an electrochemical Seebeck coefficient. The manufacturing of the tertiary batteries requires a pre-oxidation step to align and optimize the cathode and anode potentials. The pre-oxidation step, which is not part of the secondary battery manufacturing process, makes the manufacturing of tertiary batteries complex and costly. To omit the pre-oxidation step, we used partially oxidized Prussian blue analogs, i.e., $Na_xCo[Fe(CN)_6]_yzH_2O$ (Co-PBA) and $Na_xNi[Fe(CN)_6]_yzH_2O$ (Ni-PBA), as cathode and anode materials. The modified tertiary battery without the pre-oxidation step shows good thermal cyclability between 10 °C and 50 °C without detectable deterioration of the thermal voltage (V_{cell}) and discharge capacity (Q_{cell}).

Keywords: energy harvesting; thermo-rechargeable battery; tertiary battery; Prussian blue analogue; partial oxidization synthesis

1. Introduction

Energy harvesting from environmental heat is an important technology for our future society. Among the energy harvesting devices, thermo-rechargeable batteries [1–8] that can be charged by the warming/cooling of the device are promising. In thermo-rechargeable batteries, the temperature coefficient ($\alpha \equiv dV/dT$) of redox potential (V) is different between the cathode and anode. The thermo-rechargeable batteries convert thermal energy into electric energy between the low (T_L) and high (T_H) heat sources, analogously to a heat engine. Hereafter, we call the thermo-rechargeable battery composed of solid active materials a tertiary battery, because it has the same device configuration as an ion secondary battery. With an increase in the device temperature from T_L to T_H, cell voltage (v_{cell}) increases from 0 V to V_{cell} (≥ 0). The battery produces electric energy through the discharge processes at T_H. With a decrease in the device temperature to T_L, v_{cell} decreases from 0 V to $-V_{cell}$. The battery produces electric energy through the discharge processes at T_L. A tertiary battery can generate electrical energy from daily temperature cycles such as day and night or sunlight and shade. Unlike a thermo-electric conversion device that converts the temperature difference within the device into electric energy, the tertiary battery converts the temperature change of the device into electric energy. Like batteries, tertiary batteries are mobile because the device does not need to be in contact with a heat source. Thus, a tertiary battery is a device that has both mobility like a dry battery and independence from a power grid like a thermoelectric conversion device.

The thermal voltage (V_{cell}) and discharge capacity (Q_{cell}) are important performance parameters of a battery. The thermal voltage is expressed by electrode parameters as $V_{cell}^{cal} = (\alpha^+ - \alpha^-)(T_H - T_L)$, where α^+ (α^-) is α of cathode (anode) material. We emphasize that cathode and anode potentials should be the same when they are assembled into a tertiary battery. We called this potential adjustment step the pre-oxidization step. Generally, the voltage of a battery decreases as the extracted charge increases. The discharge capacity of a tertiary battery is defined as the capacity at which the voltage drop is equal to V_{cell}. Since V_{cell} of the tertiary battery is relatively small (several tens mV), the charge coefficient ($\beta \equiv -dV/dq$, where q is capacity per unit weight of active material) of V can be regarded as constant. Considering the weight ratio ($r = \frac{m^+}{m^+ + m^-}$) of the cathode ($m^+$) and anode ($m^-$) active materials, the discharge capacity per unit weight of total active material is expressed by electrode parameters as $Q_{cell}^{cal} = \frac{V_{cell}^{cal}}{\frac{\beta_+}{r} + \frac{\beta_-}{1-r}}$, where β^+ (β^-) and is β of the cathode (anode) material [7,8]. The formula tells us that Q_{cell}^{cal} is maximized when the cathode and anode potentials are optimized so that $\frac{\beta_+}{r} + \frac{\beta_-}{1-r}$ is minimized. The adjustment of the cathode and anode potential is also performed at the pre-oxidization step. Thus, the pre-oxidization step is indispensable for the fabrication of a tertiary battery.

Prussian blue analogs, $Na_x M[Fe(CN)_6]_y zH_2O$ (M-PBAs; M is divalent metal element), are promising electrode materials for lithium-ion secondary battery (LIBs) [9–14], sodium-ion secondary batteries (SIBs) [15–34], and tertiary batteries [4–6]. M-PBAs show a jungle-gym-type framework structure; the intersection points and edges are metal elements and cyano groups, respectively. The framework can accommodate Na^+ and H_2O molecules. Importantly, the accommodated Na^+ can be electrochemically moved in and out accompanying reduction and oxidation of the framework. In the reduced state of M-PBA, Fe and M takes a divalent state and each nanopore accommodates one Na^+. In the oxidization process, the valence of Fe and/or M increases to trivalent with removing Na^+ from the nanopore. Most of M-PBA in reduced state show face-centered cubic (fcc) ($Fm\bar{3}m$; $Z = 4$) or trigonal ($R\bar{3}m$; $Z = 3$) structures [35–37]. As active materials for tertiary batteries, M-PBAs have three advantages. First, they can be synthesized as precipitates from aqueous solutions. In addition, they can be synthesized at a low cost since they do not contain rare elements. Second, M-PBA and its oxidants are stable in air and in aqueous solutions. In particular, a reversible redox reaction is possible in aqueous solution. Third, M-PBA shows positive and negative α. Therefore, a tertiary battery can be composed of M-PBA with positive α and M-PBA with negative α. The α values are negative in Mn-, Ni-, Cu-, and Zn-PBAs and are positive in Fe- and Co-PBAs [38]. Among M-PBAs, Co-PBA ($\alpha = +0.57$ mV/K [38]) and Ni-PBA (-0.42 mV/K [38]) are prototypical combinations as cathode and anode materials for tertiary batteries [5], because their cycle stability is good as compared with the other combination.

The conventional tertiary battery is fabricated by four steps, i.e., (i) material synthesis, (ii) electrode fabrication, (iii) pre-oxidization of electrodes, and (iv) battery assembly (Figure 1a). Unlike LIBs/SIBs (Figure 1c), the manufacturing of tertiary batteries requires the (iii) pre-oxidation step for the following two reasons. First, the cathode and anode potentials should be the same before they are assembled into a tertiary battery, Second, the potentials should be optimized so that $\frac{\beta_+}{r} + \frac{\beta_-}{1-r}$ is minimized and Q_{cell} is maximized. In the as-grown reduced state, the potential gradient (β) against charge is significantly large because the charge curve steeply increases with q. The pre-oxidation step flattens the potential gradient. The pre-oxidization step, which is performed by electrochemical oxidization of the electrodes, makes the manufacture of tertiary batteries complex and costly. If we directly synthesize partially oxidized M-PBA, we can omit the pre-oxidation step from the manufacturing process (Figure 1b). We will call such a battery a modified tertiary battery.
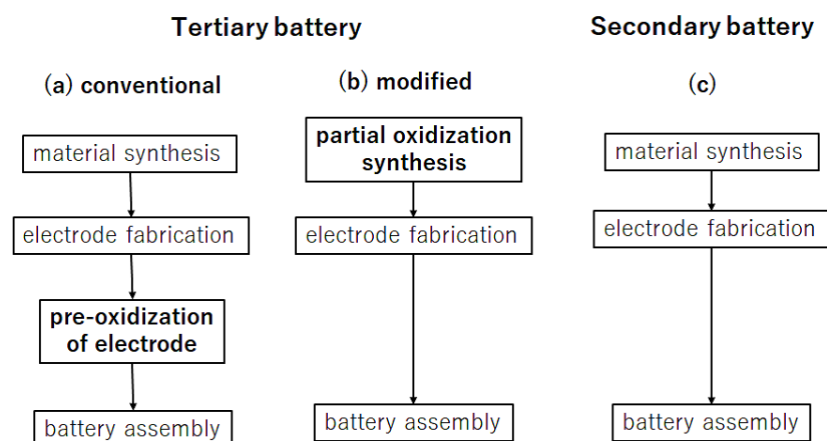
Tertiary battery

(a) conventional

material synthesis

↓

electrode fabrication

↓

pre-oxidization of electrode

↓

battery assembly

(b) modified

partial oxidization synthesis

↓

electrode fabrication

↓

battery assembly

Secondary battery

(c)

material synthesis

↓

electrode fabrication

↓

battery assembly

Figure 1. Manufacturing processes of (**a**) conventional, (**b**) modified tertiary batteries, and (**c**) secondary battery.

In this study, we performed partial oxidization synthesis of Co-PBA and Ni-PBA to omit the pre-oxidation step in the manufacturing of the tertiary batteries. The modified tertiary battery without the pre-oxidation step shows good thermal cyclability between T_L (=10 °C) and T_H (=50 °C) without detectable deterioration of V_{cell} and Q_{cell}. The V_{cell} and Q_{cell} values are close to the ideal V_{cell}^{cal} and Q_{cell}^{cal} values. By incorporating the partial oxidation synthesis, the tertiary battery can be prepared by the same processes as LIBs/SIBs and will possess an industrial advantage.

2. Materials and Methods

2.1. Partial Oxidation Synthesis

Partial oxidization synthesis of Co-PBAs and Ni-PBAs, i.e., $Na_xCo[Fe(CN)_6]_yzH_2O$ and $Na_xNi[Fe(CN)_6]_yzH_2O$, were performed by dipping solution A into solution B at a speed of 100 mL/h at 35 °C Solution A was an aqueous solution containing 10 mM MCl_2 and 4 M NaCl. Solution B was an aqueous solution containing $10(1 - n_{Fe3+}^0)$ mM $Na_4[Fe(CN)_6]$, $10n_{Fe3+}^0$ mM $K_3[Fe(CN)_6]$, and 4 M NaCl. The degree of the oxidization was controlled by the initial Fe^{3+} ratio (n_{Fe3+}^0). In preparation of solution B ($n_{Fe3+}^0 > 0.0$), K^+ in the solution was removed by an ion-exchange method. The aqueous solution containing $10(1 - n_{Fe3+}^0)$ mM $Na_4[Fe(CN)_6]$ and $10n_{Fe3+}^0$ mM $K_3[Fe(CN)_6]$ was stirred for 3 h at 50 °C with $50n_{Fe3+}^0$ mM Ni-PBA ($n_{Fe3+}^0 = 0.0$) powder. In this process, K^+ in solution exchanges with Na^+ in Ni-PBA. The ion-exchanged solutions were filtered and added 4 M NaCl.

The molar ratios of Fe and K to Co/Ni (Table 1) were determined using an SEM-EXS machine (JST-IT2000; JEOL, Ltd., Akishima, Japan). The molar ratios of C, N, and H (Table 2) were evaluated by a CHN analyzer (elementar; UNICUBE). The water content (z) was evaluated by $z = 3y\frac{m_H}{m_{CN}}$, where m_{CN} and m_H are the molar ratio of CN and H. Thus, the obtained chemical compositions of Co-PBAs and Ni-PBAs are listed in Table 3. The Fe concentration (y) ranged from 0.83 to 1.00. The molar ratio of K is less than 0.05. The Na concentration (x) was calculated from y and the degree of oxidization (p; *vide infra*) assuming charge neutrality. In the charge process of Co-PBA, Co^{2+} is oxidized first and then Fe^{3+} is oxidized [18]. Then, we formally obtained the relation $x = (1-p)(4y-2)$. In the charging process of Ni-PBA, only Fe^{2+} is oxidized [14]. Then, we obtained the relation $x = (1-p)y + (3y-2)$.

Table 1. Molar ratios of Fe and K to Co/Ni of partially-oxidized Co-PBAs and Ni-PBAs. $n^0_{\text{Fe3+}}$ are the initial Fe^{3+} ratio. Quantification of Na moles was difficult due to the weak intensity of the EDX signal.

	$n^0_{\text{Fe3+}}$	Co/Ni	Fe	K
Co-PBA	0.0	1	0.88	below the limits of detection
Co-PBA	0.6	1	0.84	0.01
Co-PBA	0.8	1	0.85	0.01
Co-PBA	1.0	1	0.88	0.02
Ni-PBA	0.0	1	0.83	below the limits of detection
Ni-PBA	0.5	1	0.86	below the limits of detection
Ni-PBA	0.9	1	0.91	below the limits of detection
Ni-PBA	1.0	1	1.00	0.05

Table 2. Weight percent of C, N, and H of partially-oxidized Co-PBAs and Ni-PBAs. The experimental error was less than 0.1 wt%. $n^0_{\text{Fe3+}}$ are the initial Fe^{3+} ratio.

	$n^0_{\text{Fe3+}}$	C (wt%)	N (wt%)	H (wt%)
Co-PBA	0.0	19.07	22.07	1.78
Co-PBA	0.6	19.08	21.75	1.96
Co-PBA	0.8	19.07	21.85	1.90
Co-PBA	1.0	19.43	22.17	1.77
Ni-PBA	0.0	17.88	20.65	2.25
Ni-PBA	0.5	18.23	20.57	2.11
Ni-PBA	0.9	18.42	20.74	2.26
Ni-PBA	1.0	18.49	20.86	2.23

Table 3. Chemical composition and lattice constant of partially-oxidized Co-PBAs and Ni-PBAs. $n^0_{\text{Fe3+}}$ and p are the initial Fe^{3+} ratio and degree of the oxidization, respectively. Fcc means face-centered-cubic cell. Subscript H means hexagonal setting.

	$n^0_{\text{Fe3+}}$	p	Composition	Structure	Lattice Constant (Å)
Co-PBA	0.0	0.00	$Na_{1.52}Co[Fe(CN)_6]_{0.88}2.96H_2O$	trigonal	$a_H = 7.428(3)$, $c_H = 17.57(1)$
Co-PBA	0.6	0.06	$Na_{1.28}Co[Fe(CN)_6]_{0.84}3.14H_2O$	fcc	$a = 10.247(4)$
Co-PBA	0.8	0.07	$Na_{1.31}Co[Fe(CN)_6]_{0.85}3.07H_2O$	fcc	$a = 10.206(3)$
Co-PBA	1.0	0.10	$Na_{1.37}Co[Fe(CN)_6]_{0.88}2.91H_2O$	fcc	$a = 10.181(3)$
Ni-PBA	0.0	0.00	$Na_{1.32}Ni[Fe(CN)_6]_{0.83}3.77H_2O$	fcc	$a = 10.290(6)$
Ni-PBA	0.5	0.10	$Na_{1.35}Ni[Fe(CN)_6]_{0.86}3.65H_2O$	fcc	$a = 10.297(4)$
Ni-PBA	0.9	0.16	$Na_{1.57}Ni[Fe(CN)_6]_{0.93}4.17H_2O$	fcc	$a = 10.291(3)$
Ni-PBA	1.0	0.15	$Na_{1.85}Ni[Fe(CN)_6]_{1.00}4.41H_2O$	fcc	$a = 10.272(4)$

Figure 2 shows the X-ray diffraction (XRD) patterns of (a) Co-PBA and (b) Ni-PBA against $n^0_{\text{Fe3+}}$. The XRD patterns were obtained using an XRD machine (MultiFlex; Rigaku) at room temperature. The X-ray source was the CuKα line. Except for Co-PBA ($n^0_{\text{Fe3+}} = 0.0$) (Figure 2a), all the diffraction peaks can be indexed in the fcc cell. For Co-PBA ($n^0_{\text{Fe3+}} = 0.0$), all the diffraction peaks can be indexed in the trigonal cell (hexagonal setting). With the use of the Rietan-FP program [39], we refined the lattice constants. The obtained lattice constants are listed in Table 3.
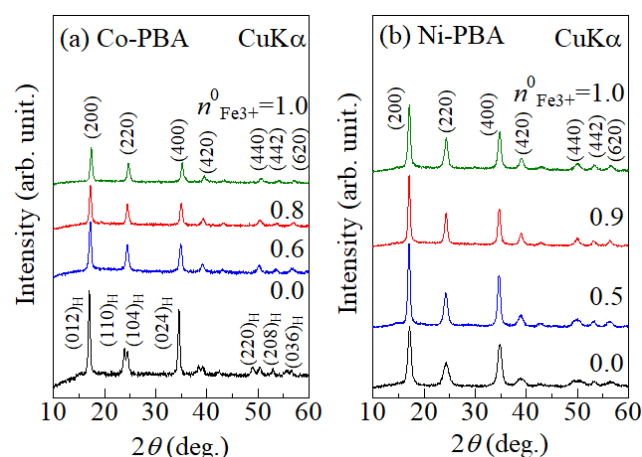
Figure 2. XRD patterns of (**a**) Co-PBA and (**b**) Ni-PBA against initial Fe^{3+} ratio (n^0_{Fe3+}). Parentheses without subscripts represent indexes in the fcc cell. Subscript H means the hexagonal setting in the trigonal cell.

2.2. Electrode Fabrication

Paste-type electrodes of Co-PBAs and Ni-PBAs were prepared as follows. First, *M*-PBA, acetylene black, and PVDF were well mixed with DMF at a ratio of 7:2:1. Then, the slurry was applied on an indium tin oxide (ITO) electrode and dried in a vacuum at 60 °C. The slurry was carefully applied by hand so that the thickness was uniform. The area of the electrode was 1.0 cm^2. To reduce the weight error, the weights of the electrodes with and without slurry were measured for each electrode. The weight of the active material, which is 70% of the slurry weight, was evaluated from the difference in the electrode weights.

We fabricated a three-pole beaker-type cell and measured charge and discharge curves with a potentiostat (HJ1001SD8; HokutoDENKO) at a rate of 0.3 C. The working, counter, and referential electrodes of the cell were the sample electrode, Pt, and Ag/AgCl standard electrodes, respectively. The electrolyte was an aqueous solution containing 17 mol/kg $NaClO_4$. We used theoretical capacity in the fully discharged state to define the C rate. The ideal capacities of Co-PBA in the fully discharged state are 122, 113, 116, and 123 mAh/g at n^0_{Fe3+} = 0.0, 0.6, 0.8, and 1.0, respectively. The currents at 1 C for a 1 mg electrode are 1.32, 1.26, 1.28, and 1.35 mA at n^0_{Fe3+} = 0.0, 0.6, 0.8, and 1.0, respectively. The ideal capacities of Ni-PBA in the fully discharged state are 67, 68, 68, and 68 mAh/g at n^0_{Fe3+} = 0.0, 0.5, 0.9, and 1.0, respectively. The currents at 1 C for a 1 mg electrode are 0.72, 0.73, 0.67, and 0.63 mA at n^0_{Fe3+} = 0.0, 0.5, 0.9, and 1.0, respectively. The potential range was from 1.1 and 0.3 V (vs. Ag/AgCl).

2.3. Battery Assembly

The Co-PBA/Ni-PBA tertiary batteries were two-pole beaker-type cell. The cathode, anode, and electrolyte were the Co-PBA electrode, Ni-PBA electrode, and aqueous solution containing 17 mol/kg $NaClO_4$, respectively. We note that Q^{cal}_{cell} (= $\frac{V^{cal}_{cell}}{\frac{\beta_+}{r} + \frac{\beta_-}{1-r}}$) is maximized when the β values of the cathode and anode are minimized. Figure 3 shows β of (a) Ni-PBA and (b) Co-PBA electrodes against V. The β values of Co-PBA and Ni-PBA are minimized at $V \approx 510$ mV (Figure 3). As will be described in the next section, Co-PBA at n^0_{Fe3+} = 1.0 and Ni-PBA at 1.0 satisfy this condition.

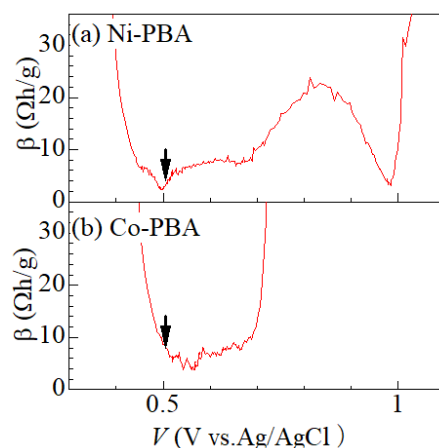**Figure 3.** Charge coefficients ($\beta = -dV/dq$) of redox potential (V) of (**a**) Ni-PBA and (**b**) Co-PBA electrodes against V. Downward arrows indicate the initial potential for the tertiary battery.

We assembled a Co-PBA(n_{Fe3+}^0 = 1.0)/Ni-PBA(1.0) tertiary battery (modified cell) without the pre-oxidation step (Figure 1b). For comparison, we assembled a conventional Co-PBA(n_{Fe3+}^0 = 0.0)/Ni-PBA(0.0) tertiary battery with the pre-oxidation step (Figure 1a). The pre-oxidization was performed with the use of the three-pole beaker-type cell. In Table 4, we summarized the electrode parameters for the modified and conventional cells.

Table 4. Parameters of cathodes and anodes for the modified and conventional cells. β^+ (β^-), m^+ (m^-), R^+ (R^-), and V^+ (V^-) are the charge coefficient ($\beta \equiv -dV/dq$) of V, the weight of active material, internal resistivity, and initial potential (vs. Ag/AgCl) of cathode (anode), respectively. The electrolyte was 17 kg/L NaClO$_4$.

Cathode	Material	β^+ (Ωg/h)	m^+ (mg)	V^+ (mV)	α^+ (mV/K)	R^+ (kΩ)
modified cell	Co-PBA	4.1	0.70	510	0.57 [38]	0.40
conventional cell	Co-PBA	5.0	0.26	520	0.57 [38]	0.71

Anode	Material	β^- (Ωg/h)	m^- (mg)	V^- (mV)	α^+ (mV/K)	R^- (kΩ)
modified cell	Ni-PBA	7.6	0.27	510	−0.42 [38]	0.74
conventional cell	Ni-PBA	5.3	0.13	520	−0.42 [38]	0.80

2.4. Thermal Cycle Measurement

The thermal cycle properties of the tertiary batteries were investigated between T_L (=10 °C) and T_H (=50 °C). The temperature (T) of the battery was controlled in a thermobath. To stabilize the potential of the electrodes, the cell was connected to an external resistor and held for several hours at T_L (=10 °C) before the measurement. The thermal cycle consists of four processes, (i) heating, (ii) discharge at T_H, (iii) cooling, and (iv) discharge at T_L. In the (i) heating process, T was slowly increased from T_L to T_H under open circuit conditions. Then, the cell was kept at T_H for 15 min to stabilize the potential. At (ii) T_H, the discharge process was investigated at 0.03 C until the v_{cell} reached 0 mV. The C rate was defined by the theoretical capacity of the Co-PBA electrode in the fully discharged state. The currents at 1 C for a 1 mg Co-PBA electrode are 1.35 and 1.32 mA for the modified and conventional cells, respectively. In the (iii) cooling process, T was slowly decreased to T_L. Then, the cell was kept at T_L for 15 min. At (iv) T_L, the discharge process was investigated at 0.03 C until v_{cell} reaches 0 mV. The thermal cycle measurements were repeated five times.

3. Results and Discussion

3.1. Degree of Oxidization

Figure 4a shows first (red) and second (blue) charge curves of partially oxidized Co-PBA at 0.3 C and 25 °C against n_{Fe3+}^0. At n_{Fe3+}^0 = 0.0, the first and second charge

curves coincide with each other. The charge curves show a two-plateau structure at ∼1.0 V and ∼0.6 V. The upper and lower plateaus are ascribed to the redox process of $[Fe(CN)_6]^{4-}/[Fe(CN)_6]^{3-}$ and Co^{3+}/Co^{2+}, respectively [18]. The observed charge capacity (=113 mAh/g) is close to the ideal value (=122 mAh/g). At n^0_{Fe3+} = 1.0, the first charge capacity (=98 mAh/g) is smaller than second charge capacity (=109 mAh/g), reflecting the the partial oxidization of Co-PBA. The first charge curve is overlapped with the second charge curve if the curve is shifted by 11 mAh/g. The partially oxidized Co-PBA (n^0_{Fe3+} = 1.0) shows initial potential of 0.50 V and is suitable for the cathode material for the Co-PBA/Ni-PBA tertiary battery. Similar behaviors are observed at n^0_{Fe3+} = 0.6 and 0.8. Figure 5a shows the first (red) and second (blue) charge curves of partially oxidized Co-PBA (n^0_{Fe3+} = 0.8) at 0.3 C and 25 °C. The first and second discharge curves coincide with each other even though the first and second charge curves (Figure 4a) differ significantly. Thus, the partially oxidized Co-PBA shows stable charge properties.

　　　Figure 4b shows the first and second charge curves of partially oxidized Ni-PBA at 0.3 C and 25 °C against n^0_{Fe3+}. At n^0_{Fe3+} = 0.0, the first and second charge curves coincide with each other. The charge curves show a single plateau structure. The plateau is ascribed to the redox process of $[Fe(CN)_6]^{4-}/[Fe(CN)_6]^{3-}$ [14]. The observed charge capacity (=54 mAh/g) is close to the ideal value (=67 mAh/g). At n^0_{Fe3+} = 1.0, the first charge capacity (=62 mAh/g) is smaller than the second charge capacity (=73 mAh/g), reflecting the partial oxidization of Ni-PBA. The first charge curve is overlapped with the second charge curve if the curve is shifted by 11 mAh/g. The partially oxidized Ni-PBA (n^0_{Fe3+} = 1.0) shows an initial potential of 0.53 V and is suitable for the anode material for the Co-PBA/Ni-PBA tertiary battery. Similar behaviors are observed at n^0_{Fe3+} = 0.5 and 0.9. Figure 5b shows the first (red) and second (blue) charge curves of partially oxidized Ni-PBA (n^0_{Fe3+} = 0.9) at 0.3 C and 25 °C. The first and second discharge curves coincide with each other even though the first and second charge curves (Figure 4b) differ significantly. Thus, the partially oxidized Co-PBA shows stable charge properties.
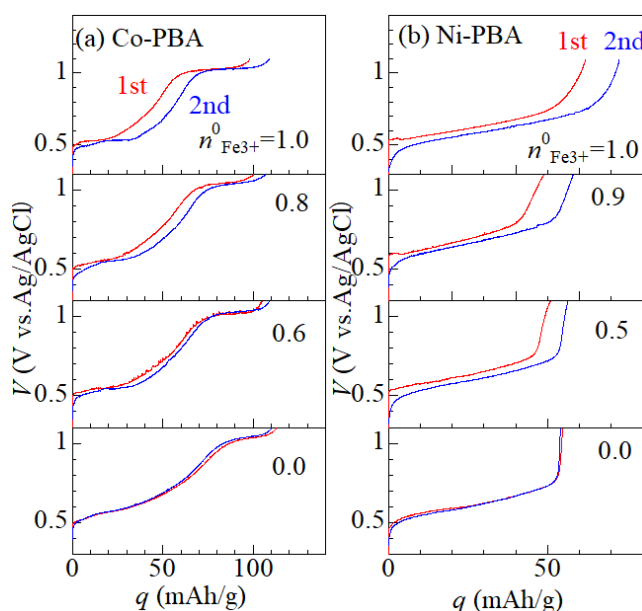

Figure 4. First (red) and second (blue) charge curves of partially oxidized (**a**) Co-PBA and (**b**) Ni-PBA at 0.3 C and at 25 °C against n^0_{Fe3+}.
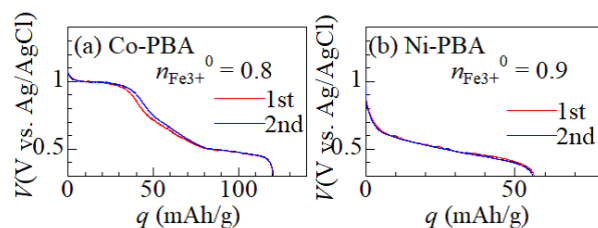
Figure 5. First (red) and second (blue) discharge curves of (**a**) Co-PBA (n^0_{Fe3+} = 0.8) and (**b**) Ni-PBA (n^0_{Fe3+} = 0.9) at 0.3 C and at 25 °C.

Here, we define the degree of oxidization (p) as the ratio between the oxidization charge and the observed capacity of the fully reduced compound. When the active material is partially oxidized, the initial capacity is the difference between the observed capacity in the fully reduced compound and the oxidation charge. The second cycle capacity corresponds to the observed capacity in the fully reduced compound. Then, p is expressed as 1- (initial capacity)/(second cycle capacity). Figure 6 shows the p values of (a) Co-PBA and (b) Ni-PBA against n^0_{Fe3+}. In both the compounds, the p value linearly increases with an increase in n^0_{Fe3+}, as indicated by straight lines. In Ni-PBA, p is proportional to the concentration of Fe^{3+} in the as-grown sample. Then, the observed proportional relationship indicates that the as-grown Ni-PBA contains Fe^{3+} in proportion to n^0_{Fe3+}. In Co-PBA, p is not directly proportional to the concentration of Fe^{3+} in the as-grown sample, since charge transfer from Co^{2+} to Fe^{3+} occurs within the sample. The observed proportional relationship is probably because the amount of charge transfer is proportional to the concentration of Fe^{3+} incorporated during crystal growth.
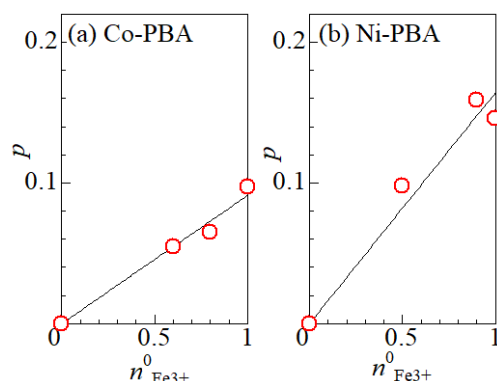

Figure 6. Degree of oxidization (p; open circles) of (**a**) Co-PBA and (**b**) Ni-PBA against n^0_{Fe3+}. Straight lines are the results of least-squares fitting.

3.2. Thermal Cycle Properties

Figure 7 shows the first thermal cycle of the modified Co-PBA/Ni-PBA tertiary battery between T_L (=10 °C) and T_H (=50 °C). The modified cell was fabricated without the pre-oxidization step (Figure 1b). In the (i) heating process, v_{cell} increases from 0 mV to 40 mV (=V_{cell}). In the (ii) discharge at T_H, v_{cell} linearly decreases from V_{cell} to 0 mV. In the (iii) cooling process, v_{cell} decreases from 0 mV to −40 mV (=−V_{cell}). In the (iv) discharge at T_L, v_{cell} linearly increases from −V_{cell} to 0 mV. Figure 7b shows the thermal cycle of the modified cell between T_L (=10 °C) and T_H (=50 °C). We observed no serious deterioration of V_{cell} and Q_{cell} up to five cycles. For comparison, we show in Figure 7c the thermal cyclability of the conventional cell.
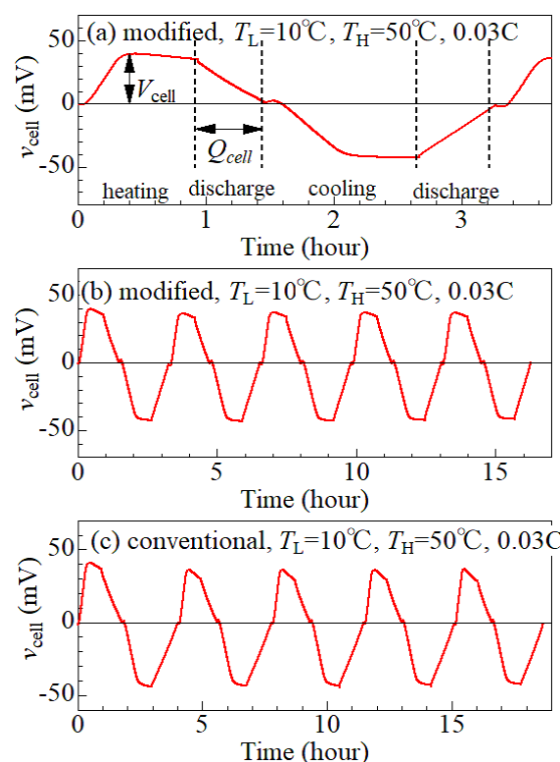
Figure 7. (**a**) The first thermal cycle of modified Co-PBA/Ni-PBA tertiary battery between T_L (= 10 °C) and T_H (= 50 °C). V_{cell} and Q_{cell} represent thermal voltage and discharge capacity, respectively. (**b**) Thermal cycle of modified cell. (**c**) Thermal cycle of conventional cell.

Figure 8a shows V_{cell} and Q_{cell} of the modified cell against cycle number. The Q_{cell} value was evaluated from the discharge time. V_{cell} and Q_{cell} are nearly constant against cycle number. We show in Figure 8b V_{cell} and Q_{cell} of the conventional cell against cycle number. V_{cell} are nearly constant against cycle number. Q_{cell}, however, gradually decreases with an increase in cycle number. Thus, the capacity cyclability of the modified cell (Figure 8a) is improved as compared with that of the conventional cell (Figure 8b).
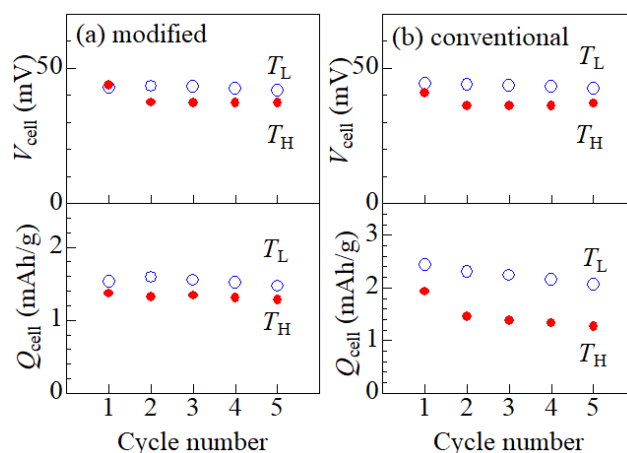

Figure 8. V_{cell} and Q_{cell} against cycle number; (**a**) modified and (**b**) conventional cells. Open and closed circles represent the data obtained at T_L (= 10 °C) and T_H (= 50 °C).

Takahara et al. [5] fabricated two tertiary batteries made of thin films of M-PBA, i.e., $Na_xCo[Fe(CN)_6]_{0.90}/Na_xCo[Fe(CN)_6]_{0.71}$ and $Na_xCo[Fe(CN)_6]_{0.90}/Na_xNi[Fe(CN)_6]_{0.68}$ cells, and investigated their thermal cyclabilities between 10 °C and 50 °C. They found that the capacity cyclability is much improved in the latter cell and ascribed the improvement

to better capacity cyclability of the $Na_xNi[Fe(CN)_6]_{0.68}$ anode at 50 °C. Then, the better capacity cyclability observed in the modified cell (Figure 8a) is considered to be ascribed to better capacity cyclability of the active materials used in the modified cell. With use of the Scherrer's equation, we evaluated the grain sizes of Co-PBAs and Ni-PBAs used in the modified and conventional cells. The grain sizes of the active materials in the modified cell were 20 nm (Co-PBA, n^0_{Fe3+} = 1.0) and 10 nm (Ni-PBA, n^0_{Fe3+} = 1.0) whereas those in the conventional cell were 100 nm (Co-PBA, n^0_{Fe3+} = 0.0) and 10 (Ni-PBA, n^0_{Fe3+} = 0.0). The smaller grain size in the modified cell is advantageous for the stable electrochemical process, and hence, the capacity cyclability.

3.3. Comparison between Observed and Calculated V_{cell} Anmd Q_{Cell}

Finally, let us compare the observed V_{cell} and Q_{cell} values with the calculated values, i.e., V^{cal}_{cell} [= $(\alpha^+ - \alpha^-)(T_H - T_L)$] and Q^{cal}_{cell} [= $\frac{\alpha^+ - \alpha^-}{\frac{\beta^+}{r} + \frac{\beta^-}{1-r}}(T_H - T_L)$] [7,8]. The electrode parameters, α^+ (α^-), β^+ (β^-), and r ($\frac{m^+}{m^+ + m^-}$), are listed in Table 4. The temperature difference (=$T_H - T_L$) is 40 K. In the modified cell, V^{cal}_{cell} and Q^{cal}_{cell} are 39.6 mV and 1.2 mAh/g, respectively. The observed V_{cell} and Q_{cell} (Figure 8a) are close to the calculated values. In the conventional cell, V^{cal}_{cell} and Q^{cal}_{cell} are 39.6 mV and 1.7 mAh/g, respectively. The observed V_{cell} values (Figure 8b) are close to the calculated value (=39.6 mV). In the conventional cell (Figure 8b), Q_{cell} at T_H is much smaller than Q_{cell} at T_L even though their average is around the calculated value (=1.7 mAh/g). We note that the difference in Q_{cell} between T_H and T_L has a serious effect on the long-term thermal stability. The cathode (anode) material in a tertiary battery is reduced (oxidized) at T_H and oxidized (reduced) at T_L. Therefore, if Q_{cell} differs significantly, the Na^+ concentration (x) of the electrode materials will change as the cycles number increases.

4. Conclusions

We proposed a modified manufacturing method for the Co-PBA/Ni-PBA tertiary battery free from the pre-oxidation step. Especially, the capacity cyclability of the modified cell between T_L (=10 °C) and T_H (=50 °C) is better than that of the conventional one. The observed V_{cell} and Q_{cell} are reproduced by the calculation based on the electrode parameters. Our method is applicable to other electrode materials and enables the manufacturing of tertiary batteries in the same steps as the commercialized LIBs. From the viewpoint of the manufacturing process and manufacturing costs, the tertiary battery is considered to be one of the promising energy harvesting devices.

Author Contributions: Conceptualization, supervision, and writing, Y.M., investigation, M.S., data curation, H.I. and I.N. All authors have read and agreed to the published version of the manuscript.

Data Availability Statement: The data presented in this study are available on request from the corresponding author.

Conflicts of Interest: The authors declare no conflict of interest.

References

1. Lee, S.W.; Yang, Y.; Lee, H.-W.; Ghasemi, H.; Kraemer, D.; Chen, G.; Cui, Y. An electrochemical system for efficiently harvesting low-grade heat energy. *Nat. Commun.* **2014**, *5*, 3942. [CrossRef] [PubMed]
2. Yang, Y.; Lee, S.W.; Ghasemi, H.; Loomis, J.; Li, X.; Kraemer, D.; Zheng, G.; Cui, Y.; Chen, G. Charging-free electrochemical system for harvesting low-grade thermal energy. *Proc. Natl. Acad. Sci. USA* **2014**, *111*, 17011–17016. [CrossRef] [PubMed]
3. Wang, J.; Feng, S.-P.; Yang, Y.; Hau, N.Y.; Munro, M.; Ferreira-Yang, E.; Chen, G. Thermal charging phenomenon in electrical double layer capacitors. *Nano Lett.* **2015**, *15*, 5784–5790. [CrossRef]

4. Shibata, T.; Fukuzumi, Y.; Kobayashi, W.; Moritomo, Y. Thermal power generation during heat cycle near room temperature. *Appl. Phys. Express* **2018**, *11*, 017101. [CrossRef]

5. Takahara, I.; Shibata, T.; Fukuzumi, Y.; Moritomo, Y. Improved thermal cyclability of tertiary battery made of Prussian blue analogues. *ChemistrySelect* **2018**, *4*, 8558–8563. [CrossRef]

6. Nagai, I.; Shimaura, Y.; Shibata, T.; Moritomo, Y. Performance of tertiary battery made of Prussian blue analogues. *Appl. Phys. Express* **2021**, *14*, 094004. [CrossRef]

7. Shimaura, Y.; Shibata, T.; Moritomo, Y. Interrelation between discharge capacity and charge coefficient of redox potential in tertiary batteries made of transition metal hexacyanoferrate. *Jpn. J. Appl. Phys.* **2022**, *61*, 044004. [CrossRef]

8. Shibata, T.; Nakamura, K.; Nozaki, S.; Iwaizumi, H.; Ohnuki, H.; Moritomo, Y. Optimization of electrode parameters of $Na_xCo[Fe(CN)_6]_{0.88}/Na_xCd[Fe(CN)_6]_{0.99}$ tertiary battery. *Sustain. Mater. Technol.* **2022**, *33*, e00483.

9. Imanishi, N.; Morikawa, T.; Kondo, J.; Takeda, Y.; Yamamoto, O.; Kinugasa, N.; Yamagishi, T. Lithium intercalation behavior into iron cyanide complex as positive electrode of lithium secondary battery. *J. Power Sources* **1999**, *79*, 215–219. [CrossRef]

10. Imanishi, N.; Morikawa, T.; Kondo, J.; Yamane, R.; Takeda, Y.; Yamamoto, O.; Sakaebe, H.; Tabuchi, M. Lithium intercalation behavior of iron cyanometallates. *J. Power Sources* **1999**, *81–82*, 530–534. [CrossRef]

11. Okubo, M.; Asakura, D.; Mizuno, Y.; Kim, J.-D.; Mizokawa, T.; Kudo, T.; Honma, I. Switching redox-active sites by valence tautomerism in prussian blue analogues $A_xMn_y[Fe(CN)_6]nH_2O$ (A = K, Rb): Robust frameworks for reversible Li storage. *J. Phys. Chem. Lett.* **2010**, *1*, 2063–2071. [CrossRef]

12. Matsuda, T.; Moritomo, Y. Thin film electrode of Prussian blue analogue for Li-ion battery. *Appl. Phys. Express* **2010**, *4*, 047101. [CrossRef]

13. Takachi, M.; Matsuda, T.; Moritomo, Y. Structural, electronic, and electrochemical properties of $Li_xCo[Fe(CN)_6]_{0.90}2.9H_2O$. *Jpn. J. Appl. Phys.* **2013**, *52*, 044301. [CrossRef]

14. Moritomo, Y.; Takachi, M.; Kurihara, Y.; Matsuda, T. Thin Fflm electrodes of Prussian blue analogues with rapid Li^+ intercalation. *Appl. Phys. Express* **2012**, *5*, 041801. [CrossRef]

15. Lu, Y.; Wang, L.; Cheng, J.; Goodenough, J.B. Prussian blue: A new framework of electrode materials for sodium batteries. *Chem. Commun.* **2012**, *48*, 6544–6546. [CrossRef]

16. Matsuda, T.; Takachi, M.; Moritomo, Y. A sodium manganese ferrocyanide thin film for Na-ion batteries. *Chem. Commun.* **2013**, *49*, 2750–2752. [CrossRef] [PubMed]

17. Takachi, M.; Matsuda, T.; Moritomo, Y. Cobalt hexacyanoferrate as cathode material for Na^+ secondary battery. *Appl. Phys. Express* **2013**, *6*, 025802. [CrossRef]

18. Takachi, M.; Matsuda, T.; Moritomo, Y. Redox reactions in Prussian blue analogue films with fast Na^+ intercalation. *Jpn. J. Appl. Phys.* **2013**, *52*, 090202. [CrossRef]

19. Yang, D.; Xu, J.; Liao, X.-Z.; He, Y.-S.; Liu, H.; Ma, Z.-F. Structure optimization of Prussian blue analogue cathode materials for advanced sodium ion batteries. *Chem. Commun.* **2014**, *50*, 13377–13380. [CrossRef]

20. Lee, H.W.; Wang, R.Y.; Pasta, M.; Lee, S.W.; Liu, N.; Cui, Y. Manganese hexacyanomanganate open framework as a high-capacity positive electrode material for sodium-ion batteries. *Nat. Commun.* **2014**, *5*, 5280. [CrossRef]

21. Wang, L.; Song, J.; Qiao, R.Q.; Wray, L.A.; Hossain, M.A.; Chuang, Y.-D.; Yang, W.; Lu, Y.; Evans, D.; Lee, J.-J.; et al. Rhombohedral Prussian white as cathode for rechargeable sodium-ion batteries. *J. Am. Chem. Soc.* **2015**, *137*, 2548–2554. [CrossRef] [PubMed]

22. You, Y.; Wu, X.-L.; Yin, Y.-X.; Guo, Y.-G.; You, Y.; Wu, X.-L.; Yin, Y.-X.; Guo, Y.-G. A zero-strain insertion cathode material of nickel ferricyanide for sodium-ion batteries. *J. Mater. Chem. A* **2013**, *1*, 14061–14065. [CrossRef]

23. Yu, S.; Li, Y.; Lu, Y.; Xu, B.; Wang, Q.; Yan, M.; Jiang, Y.A. A promising cathode material of sodium iron–nickel hexacyanoferrate for sodium ion batteries. *J. Power Sources* **2015**, *275*, 45–49. [CrossRef]

24. Xu, L.; Li, H.; Wu, X.; Shao, M.; Liu, S.; Wang, B.; Zhao, G.; Sheng, P.; Chen, X.; Han, Y.; et al. Well-defined $Na_2Zn_3[Fe(CN)_6]_2$ nanocrystals as a low-cost and cycle-stable cathode material for Na-ion batteries. *Electrochem. Commun.* **2019**, *98*, 78–81. [CrossRef]

25. Peng, J.; Zhang, W.; Liu, Q.; Wamg, J.; Chou, S.; Liu, H.; Dou, S. Prussian Blue Analogues for Sodium-Ion Batteries: Past, Present, and Future. *Adv. Mater.* **2022**, *34*, 2108384. [CrossRef]

26. Geng, W.; Zhang, Z.; Yang, Z.; Tang, H.; He, G. Non-aqueous synthesis of high-quality Prussian blue analogues for Na-ion batteries. *Chem. Commun.* **2022**, *58*, 4472–4475. [CrossRef]

27. Liu, X.; Cao, Y.; Sun, J. Defect Engineering in Prussian Blue Analogs for High-Performance Sodium-Ion Batteries. *Adv. Energy Mater.* **2022**, *12*, 2205232. [CrossRef]

28. Zhang, H.; Peng, J.; Li, L.; Zhao, Y.; Guo, Y.; Wang, J.; Cao, Y.; Dou, S.; Chou, S. Low-Cost Zinc Substitution of Iron-Based Prussian Blue Analogs as Long Lifespan Cathode Materials for Fast Charging Sodium-Ion Batteries. *Adv. Funct. Mater.* **2023**, *33*, 2210725. [CrossRef]

29. Wang, W.; Gang, Y.; Peng, J.; Hu, Z.; Yan, Z.; Lai, W.; Ahu, Y.; Appadoo, D.; Ye, M.; Cao, Y.; et al. Effect of Eliminating Water in Prussian Blue Cathode for Sodium-Ion Batteries. *Adv. Funct. Mater.* **2022**, *32*, 2111721 [CrossRef]

30. He, M.; Davis, R.; Chartouni, D.; Johnson, M.; Abplanalp, M.; Troendle, P.; Suetterlin, R.-P. Assessment of the first commercial Prussian blue-based sodium-ion battery. *J. Power Sources* **2023**, *548*, 232036. [CrossRef]

31. Wu, C.; Hu, J.; Chen, H.; Zhang, C.; Xu, M.; Zhuang, L.; Ai, X.; Qian, J. Chemical lithiation methodology enabled Prussian blue as a Li-rich cathode material for secondary Li-ion batteries. *Energy Storage Mater.* **2023**, *60*, 102803. [CrossRef]

32. Wang, P.; Li, Y.; Zhu, D.; Gong, F.; Fang, S.; Zhang, Y.; Sun, S. Treatment dependent sodium-rich Prussian blue as a cathode material for sodium-ion batteries. *Dalton Trans.* **2023**, *51*, 9622–9626. [CrossRef] [PubMed]

33. Naskar, P.; Debnath, S.; Biplab, B.; Laha, S.; Benerjee, A. High-Performance and Scalable Aqueous Na-Ion Batteries Comprising a Co-Prussian Blue Analogue Framework Positive Electrode and Sodium Vanadate Nanorod Negative Electrode for Solar Energy Storage. *ACS Appl. Energy Mater.* **2023**, *6*, 4604–4617. [CrossRef]

34. Liu, X.; Gong, H.; Han, C.; Cao, Y.; Li, Y.; Sun, J. Barium ions act as defenders to prevent water from entering Prussian blue lattice for sodium-ion battery. *Energy Storage Mater.* **2023**, *57*, 118–124. [CrossRef]

35. Buser, H.J.; Schwarzenbach, D.; Petter, W.; Ludi, A. The crystal structure of Prussian Blue: $F_4[Fe(CN)_6]_3 \cdot xH_2O$. *Inorg. Chem.* **1977**, *16*, 2704–2710. [CrossRef]

36. Herren, F.; Fischer, P.; Ludi, A.; Halg, W. Neutron diffraction study of Prussian Blue, $Fe_4[Fe(CN)_6]_3xH_2O$. Location of water molecules and long-range magnetic order. *Inorg. Chem.* **1980**, *19*, 956–1959. [CrossRef]

37. Niwa, H.; Kobayashi, W.; Shibata, T.; Nitani, H.; Moritomo, Y. Invariant nature of substituted element in metal-hexacyanoferrate. *Sci. Rep.* **2017**, *7*, 13225. [CrossRef] [PubMed]

38. Moritomo, Y.; Yoshida, Y.; Inoue, D.; Iwaizumi, H.; Kobayashi, S.; Kawaguchi, S.; Shibata, T. Origin of the material dependence of the temperature coefficient of the redox potential in coordination polymers. *J. Phys. Soc. Jpn.* **2021**, *90*, 063801. [CrossRef]

39. Izumi, F.; Momma, K. Three-dimensional visualization in powder diffraction. *Solid State Phenom.* **2007**, *130*, 15–20. [CrossRef]